PAPER

Check for updates

Light trapping by porous TiO$_2$ hollow hemispheres for high efficiency photoelectrochemical water splitting†

Yuanxing Fang, [ID] [ab] Ronan Hodgson,[a] Wei Cheat Lee,[a] Huyen Le, [ID] [a] Hon Wing Boaz Chan, [ID] [a] Hassan M. Hassan,[c] Ibrahim H. Alsohaimi,[c] Giacomo E. Canciani, [ID] [ad] Rong Qian [ID] [e] and Qiao Chen [ID] ⋆[a]

Photocatalytic water splitting has recently received increasing attention as a green fuel source. The controlled nano-geometry of the photocatalytic material can improve light harvesting. In this study, as a proof of concept, hollow hemisphere (HHS)-based films of TiO$_2$ material were created by a conventional electrospray method and subsequently applied for photoelectrochemical (PEC) water splitting. To preserve the morphology of the HHS structure, a hydrolysis precipitation phase separation method (HPPS) was developed. As a result, the TiO$_2$ HHS-based thin films presented a maximum PEC water splitting efficiency of *ca.* 0.31%, almost two times that of the photoanode formed by TiO$_2$ nanoparticle-based films (P25). The unique morphology and porous structure of the TiO$_2$ HHSs with reduced charge recombination and improved light absorption are responsible for the enhanced PEC performance. Light scattering by the HHS was demonstrated with total reflection internal fluorescence microscopy (TRIFM), revealing the unique light trapping phenomenon within the HHS cavity. This work paves the way for the rational design of nanostructures for photocatalysis in fields including energy, environment, and organosynthesis.

Introduction

The photoelectrochemical (PEC) approach has received constant attention in the fields of energy,[1,2] environment,[3,4] and many others[5,6] since the discovery of the TiO$_2$ photoanode for water splitting by Fujishima and Honda in 1972.[7] The key to PEC technology is the construction of a film on a conductive substrate, allowing light absorption and efficient charge transfer. For energy harvesting from photoexcitation, the charge mobility is normally limited. To effectively extract photoexcited electrons and holes, the film thickness has to be less than the minority carrier diffusion length. However, this significantly reduces light absorption. In addition, the extinction coefficient

for light absorption is relatively small for metal oxide materials. Hence, light will be wasted by reflection or refraction. Special nanostructures have been designed to improve light absorption without undergoing charge recombination. There have been a few reports on optical designs that induce light trapping, such as prism-shaped substrates,[8] V-aligned solar cells,[9] a patterned microlens light trap,[10,11] and a pyramidal rear reflector.[12] Alternatively, nanorod (NR) arrays or textured transparent conductive oxides (TCOs) can be deposited as an antireflective coating (ARC) to reduce light reflection.[13,14] Cai *et al.* produced quasi-omnidirectional ARCs by direct hydrothermal fabrication of TiO$_2$ NR arrays, achieving <0.5% reflection of the visible light.[15] Similar results were obtained for ZnO NR coated Si-based solar cells.[16] A layer of textured transparent conductive oxides (TCOs) was demonstrated to improve light scattering for a silicon p–i–n solar cell.[13] The light-trapping structure functions by forcing multiple internal light scattering to effectively increase the optical path length. While these elegant designs can effectively increase light absorption in devices with increased performance, many involve complex procedures and are expensive and incompatible with high-throughput production.

The hollow hemisphere (HHS) structure is a unique open dome which could improve light absorption by trapping the light within the cavity of the dome. Instead of adding an additional

[a] Department of Chemistry, School of Life Sciences, University of Sussex, Brighton, BN1 9QJ, UK. E-mail: qiao.chen@sussex.ac.uk

[b] State Key Laboratory of Photocatalysis on Energy and Environment, College of Chemistry, Fuzhou University, Fuzhou 350116, P. R. China

[c] Chemistry Department, College of Science, Jouf University, P.O. Box 2014, Sakaka, Saudi Arabia

[d] Imec, Kapeldreef 75, 3001 Leuven, Belgium

[e] National Centre for Inorganic Mass Spectrometry in Shanghai, Shanghai Institute of Ceramics, Chinese Academy of Science, Shanghai 200050, P. R. China

† Electronic supplementary information (ESI) available. See DOI: https://doi.org/10.1039/d2cp04246k

This journal is © the Owner Societies 2023

Phys. Chem. Chem. Phys., 2023, **25**, 11253–11260 | 11253

optical structure on top of the photoanode, here we synthesized the photocatalyst TiO_2 into the HHS morphology as proof of the concept. As a typical example, a nanodome structure was demonstrated by Zhu *et al.* to offer nearly complete absorption of sunlight (94 g%) for an a-Si:H solar cell with a very large short circuit current of 17.5 mA cm^{-2}.[17] The multiple internal light reflection within the dome is conducive to light absorption. To achieve the light trapping effects, several methods have been reported to synthesize TiO_2 HHSs for photocatalytic applications. Self-assembled spheres were used as a template to synthesize TiO_2 HHS film for solar cells.[18–20] However, this method was restricted to a monolayer of TiO_2 HHS thin film. The etching method was also used to fabricate TiO_2 HHS thin film to enhance the overall photoconversion efficiency, although it was difficult to control the homogeneity of the individual TiO_2 HHSs.[21] Previously, TiO_2 HHSs have been synthesized by controlling the thermodynamic (Ostwald ripening process) and kinetic (gas release) factors of thioglycolic acid treated inorganic Ti precursor, but the process was too complicated to obtain high quality hollow hemispheric morphology.[22]

Electrospray is a versatile method for synthesizing HHS.[23] In this method, metal precursors are added to a polymer solution delivered in an electric field. With a highly volatile solvent and low viscosity solution, the electric field stretches the polymer solution and breaks it into beads. A hollow structure can be formed within the beads through fast solvent evaporation. In this method, the structure and film thickness can be controlled by changing the spraying time. Since electrospray is a solution-based method, a broad range of inorganic precursors and their mixtures can be applied.[24] The applied high voltage in the electrospray encourages HHSs to form homogeneous thin films stably.[25]

Herein, as a model based on the TiO_2 photocatalyst, HHS-based thin films were synthesized as a photoanode for PEC water splitting. The HHS structure was achieved by electrospray using a polymer template. To form the TiO_2 HHS, a hydrolysis precipitation phase separation (HPPS) method was developed. A total reflection internal fluorescence microscope (TRIFM) was used to investigate the light scattering of the HHS. The maximum photoconversion efficiency obtained by the TiO_2 HHS film is around 1.04%, which presents a significant enhancement compared to flat thin films (maximum photoconversion efficiency 0.56%). The electrospray method can create a unique metal oxide HHS structure with a versatile composition for further applications in sensors, solar cells, lithium-ion batteries, super-capacitors, *etc.*

Experimental

Poly(methyl methacrylate) (PMMA, M_W = 35 000, Sigma-Aldrich) was dissolved in nitromethane (NM, Sigma-Aldrich). The concentration of PMMA was fixed at 10 wt%. Titanium isopropoxide (TTIP, Sigma-Aldrich) and acetylacetone (Sigma-Aldrich) were purchased from Sigma-Aldrich and used as the metal precursor and stabilizer, respectively. To create TiO_2 HHSs,

4 wt% TTIP and 1 wt% acetylacetone were added to the 10 wt% PMMA solutions. The solutions were mixed at room temperature for 24 hours until they became clear. For the TRIFM test, the fluorescence dye rhodamine B (2%) was mixed into the polymer solution (10 wt% PMMA).

For the electrospray process, the mixture solution was loaded into syringes having needles with inner diameters ranging from 0.159 to 0.603 mm. A syringe pump was used to maintain a constant flow rate of 2.5 mL h^{-1}. A positive bias between 5 and 30 kV was applied to the metallic needle. The electrically grounded fluorine-doped tin oxide (FTO) substrate was used as the collector. The distance between the end of the needle and the FTO substrate was kept fixed at 7 to 19 cm. The prepared HHS thin film with Ti precursor was hydrolyzed with steam (95 °C) for a certain amount of time to hydrolyze the TTIP. The thin film was then annealed at 400 °C with a ramping rate of 1 °C min^{-1}. The films were further sintered at 650 and 800 °C to control the crystal phases of the TiO_2. The calcined TiO_2 HHS thin film on the FTO substrate was used as the photoanode in PEC water splitting.

The morphologies of the porous HHSs were studied by scanning electron microscopy (SEM, JSM 820M, Jeol, Japan). The HHS diameters were measured by ImageJ software. A homemade TRIFM was used to observe the light trapping within the HHS. The crystal structures of the TiO_2 HHS samples were identified using a powder X-ray diffraction spectrometer (D500, Siemens). A Fourier-transform infrared spectrometer (FTIR, Spectrum One, PerkinElmer) with attenuated total reflectance (ATR) mode was used to study the decomposition of PMMA at elevating calcination temperatures.

The PEC water splitting performances were measured using a standard three-electrode configuration. A KCl-saturated Ag/AgCl electrode (0.1976 V_{RHE} at 25 °C) and a Pt foil were used as the reference and counter electrodes, respectively, and the TiO_2 HHS thin films on FTO were used as the photoanode. The anodic photoresponses were measured under the illumination of a solar simulator with an AM 1.5G filter. The full spectral power density (irradiance) of the light source was calibrated to 100 mW cm^{-2} using an optical power meter (Newport 1830C with 818-UV). An aqueous solution of 1.0 M KOH (pH 13.7) was used as the electrolyte.

Results and discussions

The morphology of the electrosprayed nanostructures critically depends on the strength of the polymer chain interactions, which determines the surface tension generated during the extrusion process.[23,26] Here, a relatively low molecular weight PMMA was used since it has a shorter molecular chain with less entanglement. This encourages the formation of beads instead of fibres as the weak entanglement is insufficient to balance the surface tension. NM was chosen as the solvent over dimethyl formaldehyde (DMF) due to its higher vapour pressure (35 mmHg *vs.* 3.7 mmHg). The faster vaporization of NM is essential to forming the void at the centre of the bead.[23] The outer diameter of the

11254 | *Phys. Chem. Chem. Phys.*, 2023, **25**, 11253–11260

This journal is © the Owner Societies 2023

HHS is also correlated to the strength of the entanglement, determined by the length of the polymer chain and the PMMA concentration. The average wall thickness of the HHS is determined by the evaporation rate of the solvent and the PMMA concentration.[23]

The effects of processing parameters on the HHS diameters were investigated, including orifice size, the distance between the collector and the orifice, and the applied voltage. The average outer diameter of the HHS is positively correlated with the needle diameter, as shown in Fig. S1a (ESI†). This observation is qualitatively in agreement with a previous electrospinning study on nanofibers.[26] Needles with a larger diameter form a wider Taylor cone shape and, hence, a larger HHS diameter. Fig. S1b and c (ESI†) present the diameter of the HHS as a function of the working distance and the applied voltage, respectively. Increases in the working distance and electrical potential cause a decrease in the HHS diameter. At a longer working distance, the solution jet has a longer travelling time. This offers a greater probability of the solution jet breaking down into smaller droplets. Similarly, at a higher voltage bias, the extrusion force at the tip of the needle is higher, which causes a thinning of the solution jet and, therefore, a smaller HHS diameter.

The concentration of TTIP in the polymer solution affects the morphology of the electrosprayed HHS because adding the TTIP liquid effectively reduces the viscosity of the polymer solution. Homogeneous HHS structures were obtained at a low concentration of TTIP (4 wt%), as shown in Fig. S2a (ESI†). However, when the concentration of TTIP was increased to 6 wt%, inhomogeneous, multiply-dented droplets were formed instead of an HHS structure, as shown in Fig. S2b (ESI†). A lower viscosity reduces the entanglement in the polymer solution, decreasing the integrity of the HHS.

The PMMA HHSs with TTIP were calcined to remove the polymer and convert TTIP to TiO_2 at 400 °C. The complete decomposition of PMMA at 400 °C was confirmed from the FTIR-ATR study, as shown in Fig. S3 (ESI†). Typical SEM images of TiO_2 HHSs are shown in Fig. 1. The tilted cross-sectional view in Fig. 1a reveals the homogeneously deposited TiO_2 HHS. The inset in Fig. 1a gives a precise measurement of a HHS film thickness of 21 μm after 4 hours of electrospraying. Fig. 1b is a top-view image of the TiO_2 HHS thin film. The magnified image of a single TiO_2 HHS in the inset shows some crystal facets and the nanopores on the wall of the TiO_2 HHS, confirming large-scale crystallization after calcination at 400 °C. The average size of the TiO_2 HHS is about 1.5 μm. The crystallinity of the annealed TiO_2 was ascertained by XRD, as shown in Fig. 1c. At 400 °C, a pure anatase phase (JCPDS#89-4921) was obtained. By increasing the calcination temperature to 650 °C, some anatase TiO_2 was converted to the rutile phase of TiO_2 (JCPDS#21-1276)
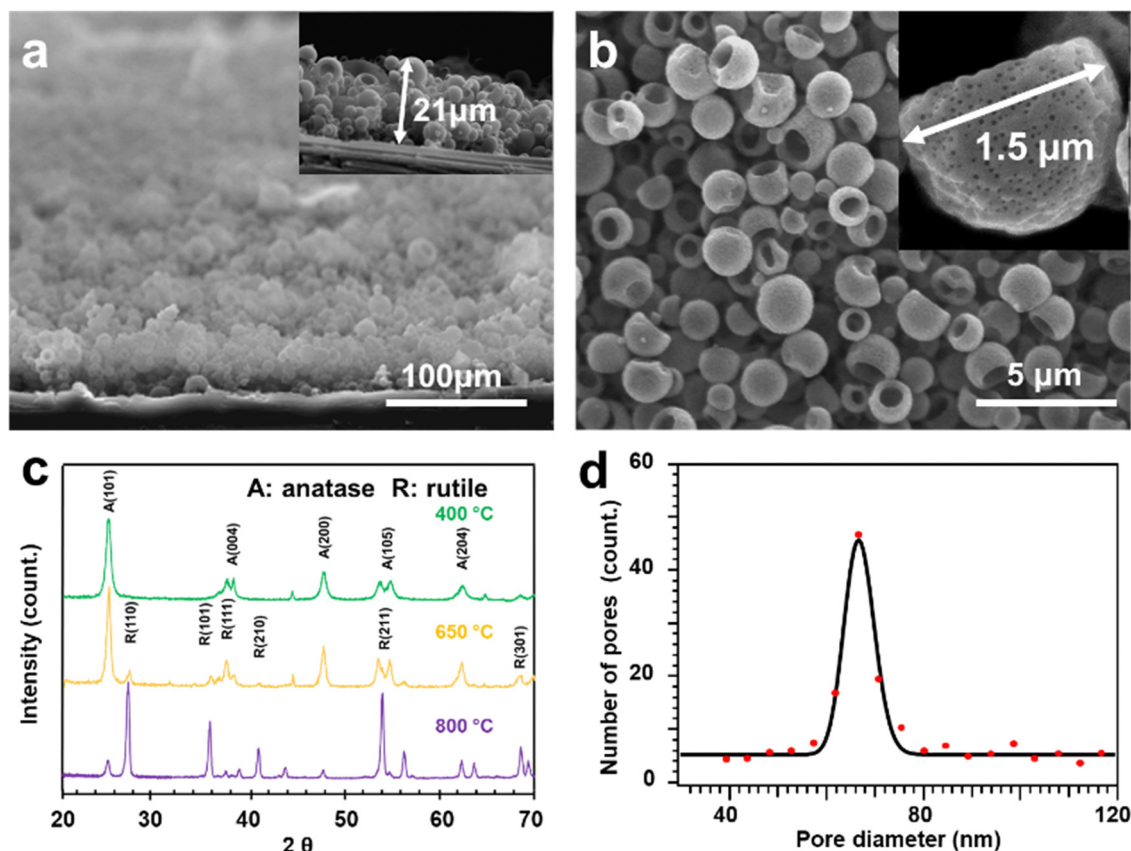
Fig. 1 Characterization of the TiO_2 HHS. (a) A tilted cross-sectional view of the TiO_2 HHSs thin films; the inset presents the film thickness. (b) A top-down SEM image of the TiO_2 HHSs; the inset is an individual HHS. (c) The XRD patterns of the TiO_2 HHSs at annealing temperatures of 400, 650 and 800 °C. (d) The average size distribution of nanopores on the surface of TiO_2 HHS.

This journal is © the Owner Societies 2023

Phys. Chem. Chem. Phys., 2023, **25**, 11253–11260 | **11255**

as it is thermodynamically more stable. When the temperature was increased to 800 °C, the rutile phase became the dominant composition. The diameter distributions of the observed nanopores were measured from the magnified SEM images (inset of Fig. 1b). The average pore diameter, displayed in Fig. 1d, is 75 nm. As shown in Fig. S2a (ESI†), these nanopores were not present before calcination. Hence, the porous structure is not due to the fast evaporation of the solvent but to the hydrolysis of TTIP and the decomposition of PMMA.

The N_2 adsorption–desorption isotherms of the porous TiO_2 HHS are shown in Fig. S4a (ESI†) with the corresponding BJH pore size distribution shown in Fig. S4b (ESI†). The isotherms are of type IV with an H1-type hysteresis loop with distinguishable capillary condensation step at $P/P_0 = 0.5$–0.9, revealing that the TiO_2 HHSs contain very uniform pore structures. The Brunauer–Emmett–Teller (BET) surface area and pore volume of the porous TiO_2 HHSs are calculated to be 9.8 m^2 g^{-1} and 0.21 cm^3 g^{-1}, respectively. This specific surface area is much smaller than that of P25 (53.6 m^2 g^{-1}) since the P25 has much smaller particle sizes.[27] The corresponding average pore size is 60 nm, which is slightly smaller than the 75 nm derived from the SEM images, suggesting that some small pores were not measured properly in the SEM images.

The morphologies of the TiO_2 HHSs are not only affected by the TTIP concentration but are also sensitive to the thermal treatment. Due to the high volatility of TTIP (melting point 17 °C and boiling point 232 °C), the morphology of PMMA HHS can be easily lost during the calcination process. Thus far, limited methods have been reported in the literature to avoid such damage.[25] To maintain the PMMA HHS morphology, an effective hydrolysis precipitation-induced phase separation method (HPPS) method was developed to convert the volatile TTIP HHSs to inorganic $Ti(OH)_4$ prior to calcination. A typical

HPPS process involves the precipitation of an inorganic phase from the organic phase by steam treatment. Once the phases are separated, further removal of the organic phase creates a porous structure in the metal oxide framework. Thus, the collapse of the HHS structure due to the vaporization of TTIP can be minimized and the morphology of PMMA HHSs can be preserved at high calcination temperatures. The titanium hydroxide is dehydrated into TiO_2 at a high temperature.

Fig. 2 shows the SEM images of the sintered TiO_2 HHSs after HPPS treatment of various durations. With little or no hydrolysis treatment (Fig. 2a and b), almost all the HHSs were destroyed by calcination. It was only after 4 hours of steam treatment that the quality of the TiO_2 HHSs was noticeably improved (Fig. 2c), as the presence of more $Ti(OH)_4$ species improves the yield of TiO_2 present after thermal treatment. At this stage, the coalescence and coagulation of HHSs can still be observed, possibly due to the melting of PMMA HHSs since there was insufficient $Ti(OH)_4$ to support the HHSs structure. The SEM image also shows that the wall of the hollow structure is much thinner than in the HHSs before calcination due to thermal evaporation and the loss of TTIP. Fig. 2d shows that the aggregation of HHSs was reduced after 6 hours of hydrolysis treatment. Although individual HHS can be recognized in the image, some coalescence can still be observed. By extending the hydrolysis treatment duration to 8 hours, the quality of TiO_2 HHSs was significantly improved (Fig. 2e), with few deformations.

These time-dependent observations highlight the importance of the hydrolysis treatment of TTIP for the formation of TiO_2 HHSs. Without converting the TTIP into $Ti(OH)_4$, the HHSs morphology will be lost during the calcination process. The limited accessibility of H_2O vapour inside the PPMA matrix means the rate of TTIP hydrolysis is slow. Hence, in a more effective HPPS method, the PMMA/TTIP HHS thin film was
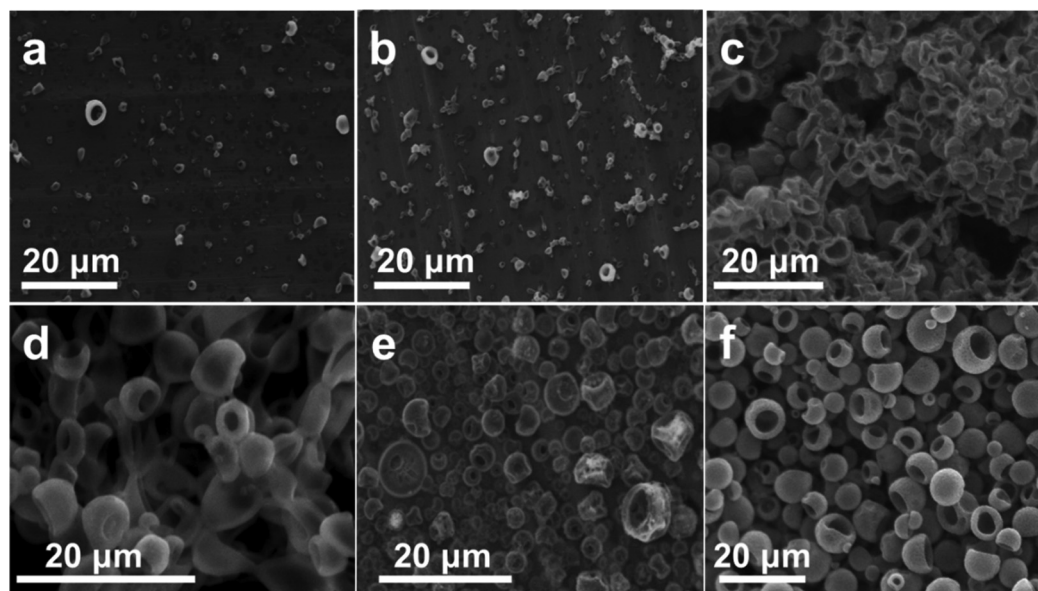

Fig. 2 Typical SEM images of sintered TiO_2 HHSs after hydrolysis lasting (a) 0 h, (b) 2 h, (c) 4 h, (d) 6 h and (e) 8 h and (f) after dipping in water followed by 1 h of hydrolysis treatment.

11256 | *Phys. Chem. Chem. Phys.*, 2023, **25**, 11253–11260

This journal is © the Owner Societies 2023

dipped in deionized water before undergoing an hour of steam treatment. The resulting excellent TiO_2 HHS morphology is shown in Fig. 2f. This improved method was used throughout this work. Similar to the conventional immersion precipitation method used to create metal oxide membranes,[28] the hydrolysis of TTIP causes phase separation, producing a porous structure. Thus, the pore size can be controlled using this HPPS method by controlling the TTIP concentration, the TTIP/PMMA ratio, and the duration/temperature of HPPS treatment. Moreover, such a method can create porous metal oxide electrospun nanofibers or metal oxide thin film if a metal precursor with polymer matrix is initially used. Such a porous texture on the HHS surface could effectively increase the density of the catalytic centres for the PEC reaction with much-improved transportation of electrolytes.

The TiO_2 HHSs thin films with 21 µm thickness were applied in PEC water splitting to evaluate the photoactivity. For comparison, P25 powder was also fabricated into a thin film using an electrophoretic deposition method,[29] with a film thickness of 20 µm, as presented in Fig. 3a. Both samples were annealed at 650 °C for an hour to obtain optimal crystallinity. As shown in Fig. 3b, the annealed TiO_2 HHSs and P25 film have almost identical XRD patterns. The measured photocurrent density as a function of the applied electrochemical potential (J–V) plot is shown in Fig. 3c. The potential was swept linearly at a scan rate of 10 mV s^{-1} between −0.9 and 0.8 $V_{Ag/AgCl}$. In the dark, the electrochemical current was negligible, indicating no electrochemical reaction. Under illumination, a steady increase of current flow was observed as the potential was increased.

The photoefficiencies of the TiO_2 HHSs and P25 thin films are plotted in Fig. 3d with the total PEC water splitting output power calculated according to the literature.[30] The maximum photoconversion efficiency under AM 1.5G is 0.27% for the HHS film, which is much higher than that for the P25 film (0.18%). Moreover, the HHS film exhibited no significant degradation of the HHS morphology after a 5 hour PEC reaction (inset of Fig. 3a).

The enhanced water splitting efficiency is likely due to the unique HHS nanostructure. The dome morphology can produce multiple light reflections within the dome to increase the optical path. To demonstrate the light trapping effects, a PMMA HHS doped with rhodamine B is excited with a laser at 523 nm under a TRIFM. Fig. 4a shows the optical image of the HHS with the corresponding fluorescence image shown in Fig. 4b recorded at the emission wavelength of 580 nm. The bright emission from rhodamine B is focused in the hollow centre of the HHS, as shown in the emission profile in Fig. 4c, indicating that the emission light was trapped within the cavity of the HHS by multiple internal reflections. Such light trapping behaviour from the HHS structure is expected to produce internal sunlight scattering with improved light absorption and enhanced photoconversion efficiency.

As the P25 film has a denser porous structure than the TiO_2 HHS film, a simple comparison cannot precisely present the advantages of the HHS film over the P25 film, even at the same film thickness. Therefore, comparisons of the photoconversion efficiency between the P25 and TiO_2 HHSs were further investigated as a function of the film thickness (Fig. 5a). The maximum PEC efficiency for P25 ($\sim$0.18% with an optimized film thickness of $\sim$20 µm) is much lower than that of the TiO_2 HHS thin film (0.31% with an optimized film thickness of 24 µm). There are three main reasons that the HHS thin films exhibit a better PEC performance. First, due to the spherical shape, TiO_2 HHS thin films have microchannels between the HHSs. This could improve the mass transportation of the
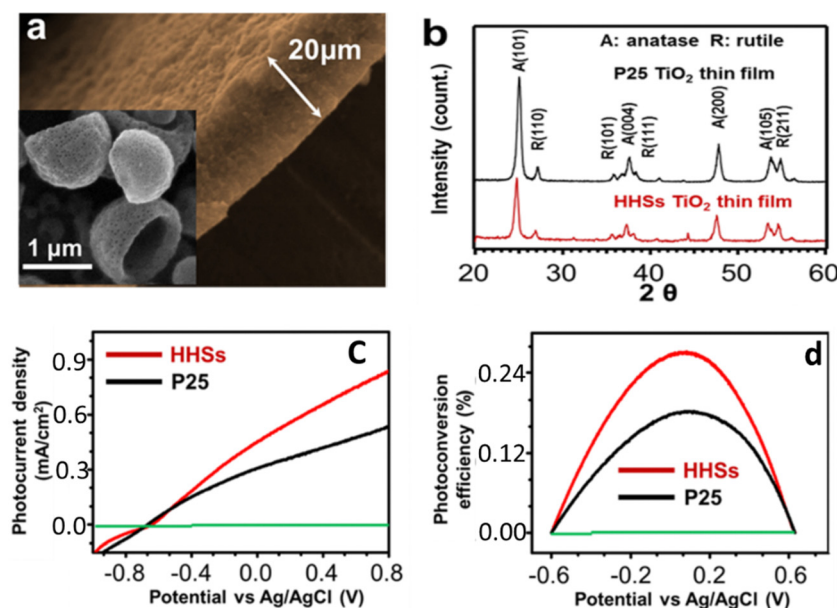

Fig. 3 (a) P25 thin film for PEC water splitting; the inset presents the maintained HHS structure after 5 hours of water splitting. (b) The XRD patterns of the TiO_2 HHSs and P25 thin film. (c) The photocurrent densities of the TiO_2 HHSs and P25 photoanodes. (d) The corresponding photoconversion efficiencies under AM 1.5G.

This journal is © the Owner Societies 2023

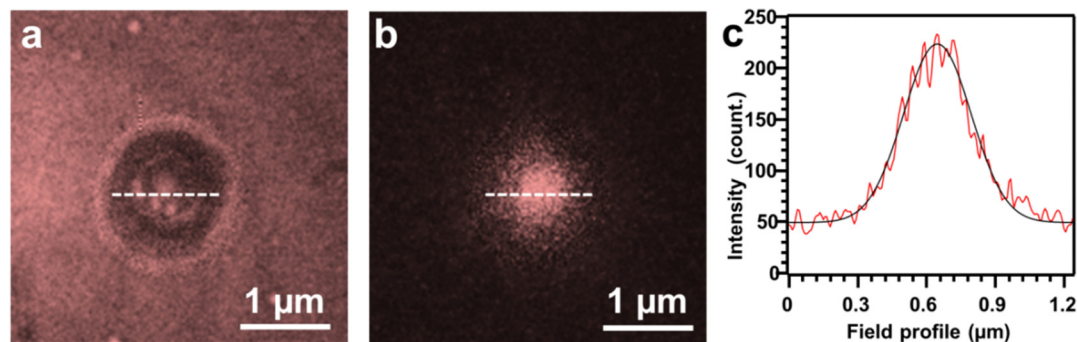*Phys. Chem. Chem. Phys.*, 2023, **25**, 11253–11260 | **11257**

Fig. 4   (a) A typical TRIFM image of PMMA HHS doped with rhodamine B. (b) The corresponding fluorescence image under excitation at 523 nm. (c) The linear profile of the light intensity corresponding to the typical sphere.
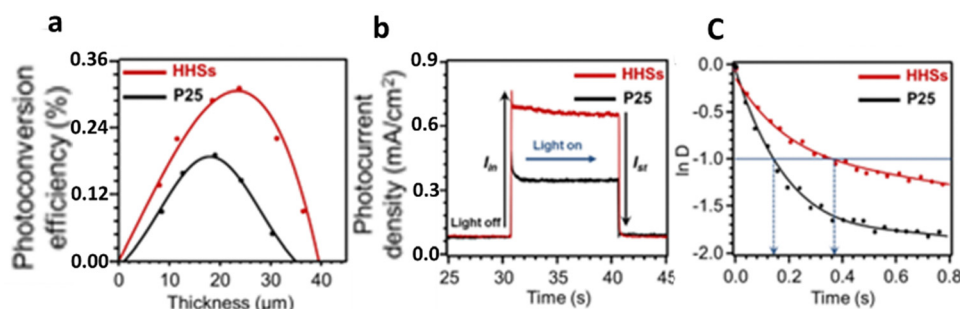

Fig. 5   (a) The photoconversion output power of the TiO_2 HHS and P25 films as a function of the film thickness under illumination. For the optimum film thicknesses, (b) the anodic photocurrent dynamics of the photoanodes and (c) the corresponding normalized plots of $\ln D$ as a function of illumination time.

electrolytes and ions in and out of the film with a larger accessible surface area of the photocatalyst. Second, the HHSs were formed with large crystal domain sizes of 21 nm, as determined from the peak width in XRD. Thus, the charge transport is expected to be improved with fewer surface defects to trap charge carriers. The nanopores in the TiO_2 HHSs formed during HPPS treatment further increase the effective surface area, offering short charge carrier diffusion pathways. Finally, and most significantly, the unique HHS morphology facilitates internal light focussing and scattering with less light reflection from the HHS film. Hence, improved light absorption, charge mobility, and liquid–solid contact are responsible for the high PEC efficiency.

Electrochemical impedance spectroscopy was performed to confirm the improved charge transfer at the interfaces between the HHSs and the electrolyte. The radius of a Nyquist plot is related to the charge transfer resistance, R_{ct}. A larger radius represents a higher interface resistance. The Nyquist plots of HHS and P25 are shown in Fig. S5 (ESI†). The charge transfer resistance of TiO_2 HHS is 18 Ω and is smaller than that of P25 (22 Ω). The smaller R_{ct} indicates that the improved crystallinity in the HHS is also responsible for the improved surface reaction kinetics.

The photoefficiency of the TiO_2 HHS film is further investigated as a function of the annealing temperature (Fig. S6, ESI†) at *ca.* 20 μm. The maximum photoconversion efficiency of

0.31% was achieved from the sample annealed at 650 °C. At a lower calcination temperature of 400 °C, the efficiency was only 0.09%. Meanwhile, after annealing at 800 °C, the photoconversion efficiency decreased to almost zero. This result can be attributed to the TiO_2 phase transition (Fig. 1c) from anatase to rutile at this high temperature. The rutile phase of TiO_2 has a direct band gap and larger effective mass for electrons and holes. Therefore, the charge recombination rate for the rutile phase is expected to be higher than that for the anatase phase, resulting in decreased PEC efficiency.

Comparison of the PEC performance with literature values is shown in Table 1. The TiO_2 HHS offers relatively superior performance among the pristine TiO_2 nanostructures. However, with doping and surface modifications, the overall PEC performance can be further improved because of surface engineering.

The initial photocurrent from both TiO_2 HHS and P25 shows an obvious anodic current spike at the point when the illumination was switched on. These current spikes are an evidence of accumulated photoexcited holes at the semiconductor–electrolyte interface.[36] They result from carrier oxidized trap states or slow oxygen evolution reaction (OER) kinetics.[37] The high density of trap states or slow OER kinetics can cause more charge recombination, resulting in a reduced stable photocurrent. Thus, the decay rate of the photocurrent in the initial spike can be used to assess the charge recombination rate. Fig. 5b compares the transient photocurrents when the light was switched on from the TiO_2 HHS

11258 | *Phys. Chem. Chem. Phys.*, 2023, **25**, 11253–11260

This journal is © the Owner Societies 2023

Table 1 Comparison of PEC performance for nanostructured TiO_2 materials

Samples	Photocurrent (mA cm^{-2}) at 1.23 V *vs.* RHE	Ref.
TiO_2 HHS	0.71	This work
Sol–gel TiO_2 film	0.60	31
TiO_2 nanorods	0.52	32
Au–TiO_2	0.65	33
$BiVO_4$ on TiO_2	0.55	34
Black phosphorus modified TiO_2 nanorods	1.2	35
Fe–TiO_2 nanorods	3.0	32
Mn–TiO_2	1.2	32

and P25 thin films at their optimized thicknesses under a constant bias of 0.4 $V_{Ag/AgCl}$. The corresponding normalised parameter (D) was calculated to estimate the recombination rate using[37–39]

$$D = (I_t - I_{st})/(I_{in} - I_{st}) \qquad (1)$$

where I_t is the current at time t, I_{in} is the initial current and I_{st} is the steady state photocurrent. The plots of $\ln D$ *vs.* t for both samples are depicted in Fig. 5c. The transient time constant (τ) is defined as the time when $\ln D = -1$, which reflects the lifetime of the minority charge carriers (holes for n-type TiO_2). The time constant for the P25 film is about 0.14 s, while for the porous TiO_2 HHS film, it is about 0.38 s. Hence, the P25 film has faster recombination than the TiO_2 HHS film, which is related to the porous structure of the highly crystallized TiO_2 HHS. Together with the improved light absorption, the overall photoconversion efficiency is improved.

Conclusions

In conclusion, a novel, porous TiO_2 HHS structure was successfully synthesized using a controlled electrospray method. The porous TiO_2 HHS-based thin films were prepared as photoanodes. An effective HPPS method was developed to accelerate the hydrolysis of TTIP and preserve the dome morphology during the calcination process. Nanopores were formed on the surface of the TiO_2 HHS due to the phase separation and the decomposition of the polymer matrix. The TRIFM image identifies the light capture within the cavity of the HHS. By optimizing the thicknesses and crystallinity of the TiO_2 HHS film, a maximum PEC efficiency of ~0.31% was achieved, significantly higher than that of the reference P25 thin films (~0.18%), under optimum conditions due to the reduced charge recombination and improved light absorption. The results confirmed that the unique morphology of the TiO_2 HHS and the structures of the film were conducive to high PEC performance. The versatile electrospray method can be used for producing HHSs with different chemical compositions which have potential in a wide range of applications.

Conflicts of interest

There are no conflicts to declare.

Acknowledgements

References

1 L. P. Qin, G. J. Wang and Y. W. Tan, *Sci. Rep.*, 2018, **8**, 16198.

2 X. C. Li, J. W. Wang, J. W. Xia, Y. X. Fang, Y. D. Hou, X. Z. Fu, M. Shalom and X. C. Wang, *ChemSusChem*, 2022, **15**, e202200330.

3 L. L. Yang, H. Chen, Y. T. Xu, R. Qian, Q. Chen and Y. X. Fang, *Chem. Eng. Sci.*, 2022, **251**, 117435.

4 S. M. Chai, X. W. Chen, X. R. Zhang, Y. X. Fang, R. S. Sprick and X. Chen, *Environ. Sci.: Nano*, 2022, **9**, 2464–2469.

5 L. Wang, X. Q. Cui, Y. T. Xu, M. Anpo and Y. Fang, *Chem. Commun.*, 2022, **58**, 10469–10479.

6 Y. W. Ma, J. Du, Y. X. Fang and X. C. Wang, *ChemSusChem*, 2021, **14**, 946–951.

7 A. Fujishima and K. Honda, *Nature*, 1972, **238**, 37–38.

8 M. Niggemann, M. Glatthaar, P. Lewer, C. Muller, J. Wagner and A. Gombert, *Thin Solid Films*, 2006, **511**, 628–633.

9 S. B. Rim, S. Zhao, S. R. Scully, M. D. McGehee and P. Peumans, *Appl. Phys. Lett.*, 2007, **91**, 243501.

10 K. Tvingstedt, S. Dal Zilio, O. Inganas and M. Tormen, *Opt. Express*, 2008, **16**, 21608–21615.

11 J. D. Myers, W. R. Cao, V. Cassidy, S. H. Eom, R. J. Zhou, L. Q. Yang, W. You and J. G. Xue, *Energy Environ. Sci.*, 2012, **5**, 6900–6904.

12 W. R. Cao, J. D. Myers, Y. Zheng, W. T. Hammond, E. Wrzesniewski and J. G. Xue, *Appl. Phys. Lett.*, 2011, **99**, 023306.

13 J. Muller, B. Rech, J. Springer and M. Vanecek, *Sol. Energy*, 2004, **77**, 917–930.

14 Y. X. Fang, D. Commandeur, W. C. Lee and Q. Chen, *Nanoscale Adv.*, 2020, **2**, 626–632.

15 J. G. Cai, J. F. Ye, S. Y. Chen, X. W. Zhao, D. Y. Zhang, S. Chen, Y. R. Ma, S. Jin and L. M. Qi, *Energy Environ. Sci.*, 2012, **5**, 7575–7581.

16 B. Hussain, A. Ebong and I. Ferguson, *Sol. Energy Mater. Sol. Cells*, 2015, **139**, 95–100.

17 J. Zhu, C. M. Hsu, Z. F. Yu, S. H. Fan and Y. Cui, *Nano Lett.*, 2010, **10**, 1979–1984.

18 S. C. Yang, D. J. Yang, J. Kim, J. M. Hong, H. G. Kim, I. D. Kim and H. Lee, *Adv. Mater.*, 2008, **20**, 1059–1064.

19 H. G. Moon, H. W. Jang, J. S. Kim, H. H. Park and S. J. Yoon, *Electron. Mater. Lett.*, 2010, **6**, 135–139.

20 H. G. Moon, Y. S. Shim, H. W. Jang, J. S. Kim, K. J. Choi, C. Y. Kang, J. W. Choi, H. H. Park and S. J. Yoon, *Sens. Actuators, B*, 2010, **149**, 116–121.

21 J. W. Lu, P. Zhang, A. Li, F. L. Su, T. Wang, Y. Liu and J. L. Gong, *Chem. Commun.*, 2013, **49**, 5817–5819.

22 C. C. Jia, P. Yang, H. S. Chen and J. P. Wang, *CrystEngComm*, 2015, **17**, 2940–2948.

23 J. Liu, A. Rasheed, H. M. Dong, W. W. Carr, M. D. Dadmun and S. Kumar, *Macromol. Chem. Phys.*, 2008, **209**, 2390–2398.

24 I. S. Chronakis, *J. Mater. Process. Technol.*, 2005, **167**, 283–293.

25 S. Park, J. B. Kim, S. Lee, J. H. Bang and Y. S. Kim, *Mater. Lett.*, 2012, **69**, 34–36.

This journal is © the Owner Societies 2023

Phys. Chem. Chem. Phys., 2023, **25**, 11253–11260 | **11259**

26 J. S. Bedi, D. W. Lester, Y. X. Fang, J. F. C. Turner, J. Zhou, S. M. Alfadul, C. Perry and Q. Chen, *J. Polym. Eng.*, 2013, **33**, 453–461.

27 S. H. Pu, D. B. Long, Z. H. Liu, F. Y. Yang and J. M. Zhu, *Catalysts*, 2018, **8**, 189.

28 B. Wang, Z. T. Wu, A. G. Livingston and K. Li, *J. Membr. Sci.*, 2009, **339**, 5–9.

29 Y. X. Fang, W. C. Lee, G. E. Canciani, T. C. Draper, Z. F. Al-Bawi, J. S. Bedi, C. C. Perry and Q. Chen, *Mater. Sci. Eng., B*, 2015, **202**, 39–45.

30 W. C. Lee, Y. X. Fang, R. Kler, G. E. Canciani, T. C. Draper, Z. T. Y. Al-Abdullah, S. M. Alfadul, C. C. Perry, H. Y. He and Q. Chen, *Mater. Chem. Phys.*, 2015, **149**, 12–16.

31 D. Regonini, A. C. Teloeken, A. K. Alves, F. A. Berutti, K. Gajda-Schrantz, C. P. Bergmann, T. Graule and F. Clemens, *ACS Appl. Mater. Interfaces*, 2013, **5**, 11747–11755.

32 C. Z. Wang, Z. Chen, H. B. Jin, C. B. Cao, J. B. Li and Z. T. Mi, *J. Mater. Chem. A*, 2014, **2**, 17820–17827.

33 R. Reichert, Z. Jusys and R. J. Behm, *J. Phys. Chem. C*, 2015, **119**, 24750–24759.

34 S. Ho-Kimura, S. J. A. Moniz, A. D. Handoko and J. W. Tang, *J. Mater. Chem. A*, 2014, **2**, 3948–3953.

35 Y. M. Xu, X. Wang, M. L. Jin, K. Kempa and L. L. Shui, *ChemElectroChem*, 2020, **7**, 96–104.

36 F. Le Formal, N. Tetreault, M. Cornuz, T. Moehl, M. Gratzel and K. Sivula, *Chem. Sci.*, 2011, **2**, 737–743.

37 Z. D. Li, C. H. Yao, Y. H. Yu, Z. Y. Cai and X. D. Wang, *Adv. Mater.*, 2014, **26**, 2262–2267.

38 A. Hagfeldt, H. Lindstrom, S. Sodergren and S. E. Lindquist, *J. Electroanal. Chem.*, 1995, **381**, 39–46.

39 Y. H. Ng, A. Iwase, A. Kudo and R. Amal, *J. Phys. Chem. Lett.*, 2010, **1**, 2607–2612.

11260 | *Phys. Chem. Chem. Phys.*, 2023, **25**, 11253–11260

This journal is © the Owner Societies 2023